# Joint regional uptake quantification of thorium-227 and radium-223 using a multiple-energy-window projection-domain quantitative SPECT method

## Supplementary Material

Zekun Li, Nadia Benabdallah, Richard Laforest, Richard L. Wahl, Daniel L. J. Thorek, Abhinav K. Jha*, *Senior Member, IEEE*

## I. Validating the SPECT simulation

### A. Experiments

SIMIND is a Monte Carlo (MC) approach that has already been shown to model single-photon emission computed tomography (SPECT) imaging systems accurately [1]–[3], including when imaging other $\alpha$-particle-emitting isotopes [4]. To demonstrate the accuracy of the SIMIND-based simulation approach for $^{227}\mathrm{Th}$-based $\alpha$-particle radiopharmaceutical therapies ($\alpha$-RPT) SPECT, we compared the projection data and energy spectra obtained with our simulation approach to that obtained on a physical scanner.

To compare simulated and physically acquired projection data, we used a NEMA phantom (Data Spectrum$^{\mathrm{TM}}$, USA). The spheres of this phantom were filled with $^{227}\mathrm{Th}$ solutions with an activity concentration of 40 kBq/ml. The rest of the phantom was filled with water to simulate attenuation and scatter due to soft tissue. The phantom was scanned on a GE Discovery 670 SPECT/CT system with a medium energy general purpose (MEGP) collimator one day after purifying the $^{227}\mathrm{Th}$ isotope and filling the isotope in the phantom. Thus, at the time of scanning, a small portion of the $^{227}\mathrm{Th}$ had decayed to $^{223}\mathrm{Ra}$. During imaging, projections were acquired in two energy windows, corresponding to the two major photopeaks of $^{223}\mathrm{Ra}$ (66 - 98 keV) and $^{227}\mathrm{Th}$ (217 - 260 keV) at 60 angular positions spaced uniformly over 360°. The same image-acquisition process was modeled using our simulation approach (Sec. III B in the main manuscript). In the simulation, the concentration of $^{227}\mathrm{Th}$ and $^{223}\mathrm{Ra}$ were calculated theoretically, based on the filling and scanning time. The profiles of the projection data obtained with the physical scanner and with the simulation approach from the two energy windows were compared.

To demonstrate the accuracy of the SIMIND-based approach in simulating the emission spectra of $^{227}\mathrm{Th}$ and $^{223}\mathrm{Ra}$ and in simulating the energy resolution of the SPECT system, we compared the simulated and physically acquired energy spectra of each isotope. First, we measured the energy spectrum of each isotope on the GE Discovery 670 SPECT/CT system equipped with a high energy genera purpose (HEGP) collimator one day after purification. For imaging each isotope, we placed the source inside a 5 ml glass vial in the center of the field of view, a point 17 cm from both heads of the scanner. We acquired projections for 5 minutes at only two opposite angular positions using the dual-head system. Energy windows, as presented in Table I, were selected to provide coverage of the relevant photopeaks for each isotope. Next, we simulated the same image-acquisition process using our SIMIND-based approach (Sec. III B in the main manuscript). In this simulation, we assumed $^{223}\mathrm{Ra}$ and its daughters were at radioactive equilibrium. The activity of $^{227}\mathrm{Th}$ and $^{223}\mathrm{Ra}$ in each source was estimated based on the acquired projections. We also simulated the stray-radiation-related noise in this process. To model the level of this noise, we estimated the mean value of stray-radiation-related noise in each projection bin for each energy window from the corresponding physically acquired projections. This was achieved by averaging the values of pixels close to the edge of the field of view. We chose these pixels because they were far from the vial and were expected to contain only stray-radiation-related noise.

Z. Li is with the Department of Biomedical Engineering, Washington University, St. Louis, MO 63130 USA.
N. Benabdallah, R Laforest, and R. L. Wahl are with the Mallinckrodt Institute of Radiology, Washington University, St. Louis, MO 63110, USA
D. L. J. Thorek is with the Department of Biomedical Engineering, Mallinckrodt Institute of Radiology, and Program in Quantitative Molecular Therapeutics, Washington University, St. Louis, MO, 63130 USA
*A. K. Jha is with the Department of Biomedical Engineering and Mallinckrodt Institute of Radiology, Washington University, St. Louis, MO 63130 USA (e-mail: a.jha@wustl.edu).

TABLE I: Energy window settings for isotope spectra acquisition

| Window Index | Range (keV) | Window Index | Range (keV) | Window Index | Range (keV) | Window Index | Range (keV) |
|---|---|---|---|---|---|---|---|
| 1 | 57.6 - 62.4 | 9 | 95.0 - 105.0 | 17 | 191.0 - 209.0 | 25 | 290.0 - 300.0 |
| 2 | 62.5 - 67.5 | 10 | 105.1 - 115.1 | 18 | 210.1 - 229.9 | 26 | 300.1 - 310.1 |
| 3 | 67.6 - 72.6 | 11 | 115.2 - 124.8 | 19 | 230.0 - 240.0 | 27 | 310.2 - 320.0 |
| 4 | 72.7 - 77.5 | 12 | 124.9 - 133.8 | 20 | 240.1 - 249.9 | 28 | 320.1 - 330.1 |
| 5 | 77.6 - 82.4 | 13 | 135.4 - 144.4 | 21 | 250.0 - 260.0 | 29 | 330.2 - 340.0 |
| 6 | 82.5 - 87.5 | 14 | 144.8 - 155.2 | 22 | 260.1 - 270.1 | 30 | 340.7 - 379.9 |
| 7 | 87.6 - 92.0 | 15 | 155.4 - 170.0 | 23 | 270.2 - 280.0 | 31 | 380.0 - 425.6 |
| 8 | 92.1 - 94.9 | 16 | 170.5 - 189.5 | 24 | 280.1 - 289.1 | 32 | 425.7 - 474.7 |

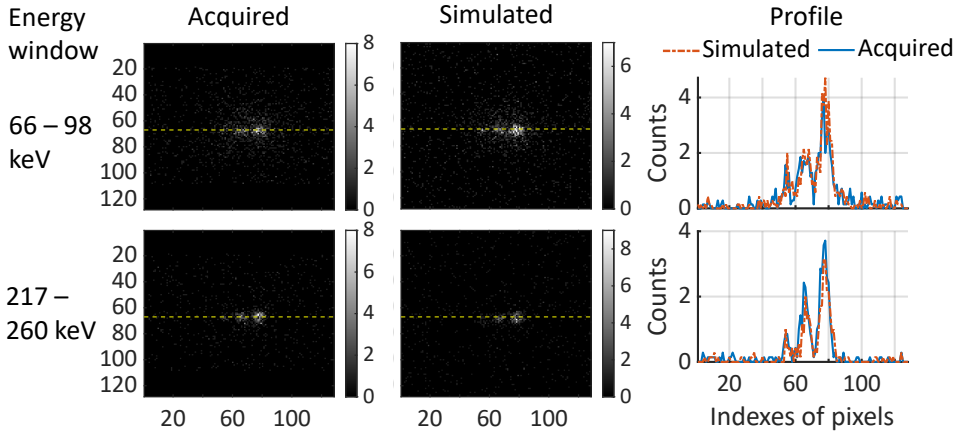


Fig. 1: Comparison of the simulated and physical-SPECT-system-acquired projections of the NEMA phantom in two different energy windows.

### B. Results

Fig. 1 shows projections of the NEMA phantom in the two energy windows at the first angular position, acquired using simulated and physical SPECT systems. We also compared the profiles along the dashed line in the projections from the two approaches in both energy windows. To reduce the noise-related variation in this profile, each point in the profile was obtained by averaging the number of counts along five adjacent pixels on both sides of the dashed line. We observed that the profile of the simulated projection matched that acquired on the physical scanner in both energy windows. This provides evidence of the accuracy of the process to simulate isotope emission, the SPECT system, and the noise in this study.

Fig. 2 presents both physically acquired and simulated spectra of $^{227}$Th and $^{223}$Ra. The spectra were generated by dividing the total counts acquired in each energy window by the window width and plotting these values against the center of each energy window. Each spectrum has been normalized such that its peak value is unity. We observe that the simulated and physically acquired spectra matched for both isotopes. Those spectra were different from simply convoluting the emission spectra of the isotopes with the energy resolutions since there were significant amounts of stray-radiation-related noise and there was a finite number of energy windows.

## II. Image Reconstruction-Based Methods Compared

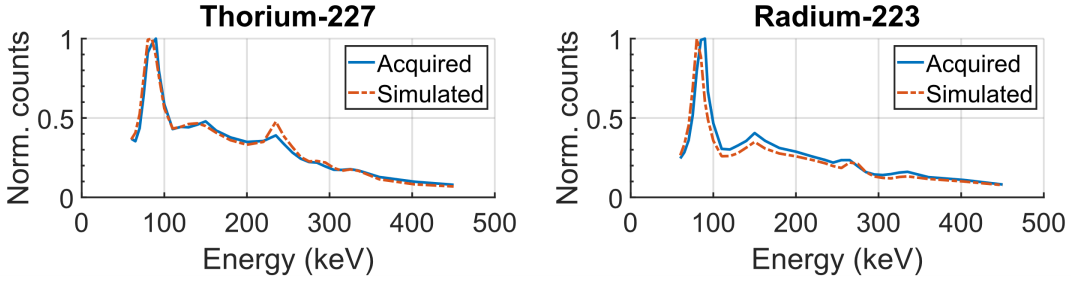


Fig. 2: Comparison of the simulated and physical-SPECT-system-acquired spectra of $^{227}$Th and $^{223}$Ra.

### A. Dual-isotope ordered subset expectation maximization image reconstruction (DOSEM)-based method

Based on analysis of the emission spectra of both isotopes, energy windows 66 - 96 keV and 217 - 260 keV (energy windows 1 and 3 in Fig. 1 of the main manuscript) were considered as the primary energy windows of $^{223}\mathrm{Ra}$ and $^{227}\mathrm{Th}$, respectively. We first reconstructed images of activity uptake of $^{227}\mathrm{Th}$ and $^{223}\mathrm{Ra}$ using projections from the corresponding two separate primary energy windows. In this step, we assumed there was no crosstalk contamination, i.e., the counts in the two energy windows solely reflected emissions from $^{227}\mathrm{Th}$ and $^{223}\mathrm{Ra}$, respectively. The images were reconstructed using the ordered subset expectation maximization (OSEM) method, implemented using Customizable and Advanced Software for Tomographic Reconstruction (CASToR) software [5]. In this process, we compensated for attenuation, scatter, collimator-detector response, stray-radiation-related noise, and the complicated emission spectra of both isotopes. The scatter was compensated using effective scatter source estimation (ESSE) method, in which the scatter kernels were generated using SIMIND simulations [6]. Next, the reconstructed image of each isotope was forward projected to the photopeak energy window of the other isotope to estimate the crosstalk contamination in each photopeak energy window. In this forward projection, we modeled the emission spectra of both isotopes, attenuation, scatter, and collimator-detector response. In this step, the crosstalk contamination from primary photons was modeled from the emission spectrum, and the crosstalk contamination from scattered photons was modeled with the ESSE method. Then, the images of both isotopes were again reconstructed using the OSEM method, with the estimated crosstalk contamination as additive correction terms. Since the estimates of crosstalk contamination were not accurate due to the inaccurate reconstruction in the first step, we repeated these steps for multiple iterations.

More specifically, we denote the process of reconstructing and forward projecting the images of both isotopes to compensate for crosstalk as a 'joint iteration'. The iterations executed specifically for each isotope in the OSEM reconstruction are referred to as 'isotope-specific iterations'. For the purpose of fine-tuning the DOSEM-based method, we sought the optimal number of joint iterations and isotope-specific iterations. To this end, we generated 50 noise realizations of a representative patient phantom. Initially, image of each isotope was reconstructed from its corresponding photopeak energy window using the OSEM-based method, incorporating ideal crosstalk corrections. Through this process, we determined that the optimal number of isotope-specific iterations was 20, each comprising 6 subsets. With this number of isotope-specific iterations, the normalized root mean square error (NRMSE) between the true and estimated lesion uptake from the reconstructed images of both isotopes converged to its lowest value. Convergence was defined as a change in NRMSE of less than 1% over the next 10 iterations. Subsequently, we performed the DOSEM-based reconstruction from the crosstalk-contaminated SPECT projections as outlined above. The optimal number of joint iterations was established at 5, ensuring that changes in the mean estimated uptake of each isotope in each region were less than 0.1% with additional joint iterations.

### B. Geometric transfer matrix (GTM)-based method

Partial volume effects (PVEs) are known to degrade quantification accuracy in SPECT [7]. The proposed method implicitly assumes constant uptake within each volume of interest (VOI). Under this assumption, PVEs can also be compensated for post-reconstruction. We compared our approach to the widely used geometric transfer matrix (GTM)-based method [8]. For each isotope, the elements of GTM were calculated from the reconstructed projections of the VOIs, obtained as described in Sec. III A of the main manuscript. Additional implementation details of this method are described in [8].

## III. Figures of merit

For a range of experimental conditions, we generated multiple instances of projection data for a single phantom, where each instance corresponded to separate noise realizations. Denote the total number of realizations by $R$. Considering one of the isotopes, denote the true activity uptake of the $k^{th}$ VOI by $\lambda_k$ and the corresponding estimate with the $r^{th}$ noise realization by $\hat{\lambda}_{rk}$. In these experiments, the accuracy of the estimated uptake of this isotope was quantified using the normalized bias (NB), which, for the $k^{th}$ VOI, is given by

$$\mathrm{NB}_k = \frac{1}{R}\sum_{r=1}^{R}\frac{\hat{\lambda}_{rk}-\lambda_k}{\lambda_k}. \tag{1}$$

The precision of the estimated uptake of this isotope was quantified using the normalized standard deviation (NSD), which, for the $k^{th}$ VOI, is given by

$$\mathrm{NSD}_k = \sqrt{\frac{1}{R-1}\sum_{r=1}^{R}\left(\frac{\hat{\lambda}_{rk}}{\lambda_k}-\frac{1}{R}\sum_{r'=1}^{R}\frac{\hat{\lambda}_{r'k}}{\lambda_k}\right)^2}. \tag{2}$$

Finally, the overall error in estimating the uptake was quantified by the normalized root mean square error (NRMSE). For the $k^{th}$ VOI,

$$\mathrm{NRMSE}_k = \sqrt{NB_k^2 + NSD_k^2}. \tag{3}$$

Multiple experiments in this study were conducted across a plural number of patients. To evaluate the performance of the methods over a population of patients, each with one or multiple noise realizations, we used the ensemble NB and ensemble

TABLE II: The performance of the MEW-PDQ and LC-QSPECT methods on the task of quantifying regional uptake of $^{227}$Th and $^{223}$Ra in $^{227}$Th-based $\alpha$-RPTs.

| | $^{223}$Ra | | | | $^{227}$Th | | | |
|---|---|---|---|---|---|---|---|---|
| NB (%) | Background | Bone | Gut | Lesion | Background | Bone | Gut | Lesion |
| MEW-PDQ | -0.03 | -1.2 | 0.05 | 0.8 | 0.01 | 1.1 | -0.3 | 0.4 |
| LC-QSPECT | 250.8 | 178.8 | 154.4 | 450.0 | 6.3 | 2.9 | 7.9 | 1.8 |
| NRMSE (%) | Background | Bone | Gut | Lesion | Background | Bone | Gut | Lesion |
| MEW-PDQ | 2.0 | 9.5 | 1.1 | 18.9 | 0.9 | 4.7 | 0.8 | 3.6 |
| LC-QSPECT | 250.8 | 179.0 | 154.4 | 450.3 | 6.4 | 5.2 | 7.9 | 3.9 |

NRMSE. We denote the number of samples in the population by $S$ and the number of noise realizations for each patient sample by $R$, and denote the true and estimated activity uptake of a particular isotope in the $k^{\text{th}}$ VOI for the $s^{\text{th}}$ sample from the $r^{th}$ realization by $\lambda_{sk}$ and $\hat{\lambda}_{skr}$, respectively. The ensemble NB for the $k^{th}$ VOI is given by

$$\text{Ensemble NB}_k = \frac{1}{SR}\sum_{s=1}^{S}\sum_{r=1}^{R}\frac{\hat{\lambda}_{skr}-\lambda_{sk}}{\lambda_{sk}}. \tag{4}$$

The ensemble NRMSE for the $k^{th}$ VOI is given by

$$\text{Ensemble NRMSE}_k = \sqrt{\frac{1}{SR}\sum_{s=1}^{S}\sum_{r=1}^{R}\left(\frac{\hat{\lambda}_{skr}-\lambda_{sk}}{\lambda_{sk}}\right)^2}. \tag{5}$$

Additionally, to quantify performance in cases where we had just a single estimate, we used normalized error, defined as the difference between the estimated and true uptake values, normalized by the true uptake value.

Finally, we also computed the Cramér-Rao lower bound (CRLB), which is the minimum variance that can be achieved by an unbiased estimator, as a benchmark for the precision of the activity estimated using the proposed method. The CRLB is given by the diagonal elements of the inverse of the Fisher information matrix for the estimated parameter. We denote the Fisher information matrix by $\boldsymbol{F}$ [9]. Since the task is to estimate regional uptake of $^{227}$Th and $^{223}$Ra at the same time, the Fisher information matrix needs to consider both isotopes. We denoted $\lambda_l$ and $\hat{\lambda}_l$ as the true and estimated activity uptake respectively, where $l$ ranges over the two isotopes in $K$ VOIs. Thus the Fisher information matrix is a $2K$ by $2K$ matrix with elements given by

$$F_{l_1 l_2} = -E\left[\frac{\partial^2}{\partial\lambda_{l_1}\partial\lambda_{l_2}}\ln\Pr(\boldsymbol{g}|\boldsymbol{\lambda})\right], \tag{6}$$

where $E[x]$ denotes the expectation of a random variable $x$. We have already derived the likelihood of the measured data $\mathbf{g}$ in the main manuscript:

$$\Pr(\mathbf{g}|\boldsymbol{\lambda}) = \prod_{m=1}^{M}\exp[-(\boldsymbol{H}\boldsymbol{\lambda})_m-\psi_m]\frac{[(\boldsymbol{H}\boldsymbol{\lambda})_m+\psi_m]^{g_m}}{g_m!}. \tag{7}$$

Substituting Eq. (7) in Eq. (6) yields

$$F_{l_1 l_2} = \sum_{m=1}^{M}\frac{H_{ml_1}H_{ml_2}}{(\boldsymbol{H}\boldsymbol{\lambda})_m+\psi_m}. \tag{8}$$

## IV. Performance of the LC-QSPECT in $^{227}$Th-based $\alpha$-RPT

### A. Experiments

In our previous studies [4], we proposed the low-count quantitative SPECT (LC-QSPECT) method to estimate the regional uptake of a single isotope from its photopeak energy window projections. The method has been observed to accurately and precisely estimate the regional uptake for patients administered with $^{223}$Ra-based $\alpha$-RPTs. Therefore, in this experiment, we evaluate the performance of the LC-QSPECT method on quantifying the regional uptake of $^{227}$Th and $^{223}$Ra for patients undergoing $^{227}$Th-based $\alpha$-RPT.

For this purpose, as described in Sec. III C of the main manuscript, we considered a patient phantom with average patient size, a 33.75 mm diameter lesion in the pelvis, standard total uptake, and regional uptake ratios as presented in Table 1 of the main manuscript. As described in Sec. III B of the main manuscript, we generated 50 noise realizations of that patient. We estimated the regional uptake of $^{227}$Th and $^{223}$Ra from those noise realizations using both the LC-QSPECT and the proposed multiple-energy-window projection-domain quantification (MEW-PDQ) methods. More specifically, the LC-QSPECT method was applied to individually estimate the regional uptake of $^{223}$Ra and $^{227}$Th from their respective photopeak energy windows, without accounting for crosstalk contamination. More implementation details of the LC-QSPECT method are described in [4]. The MEW-PDQ method was applied as described in Sec. III A of the main manuscript.

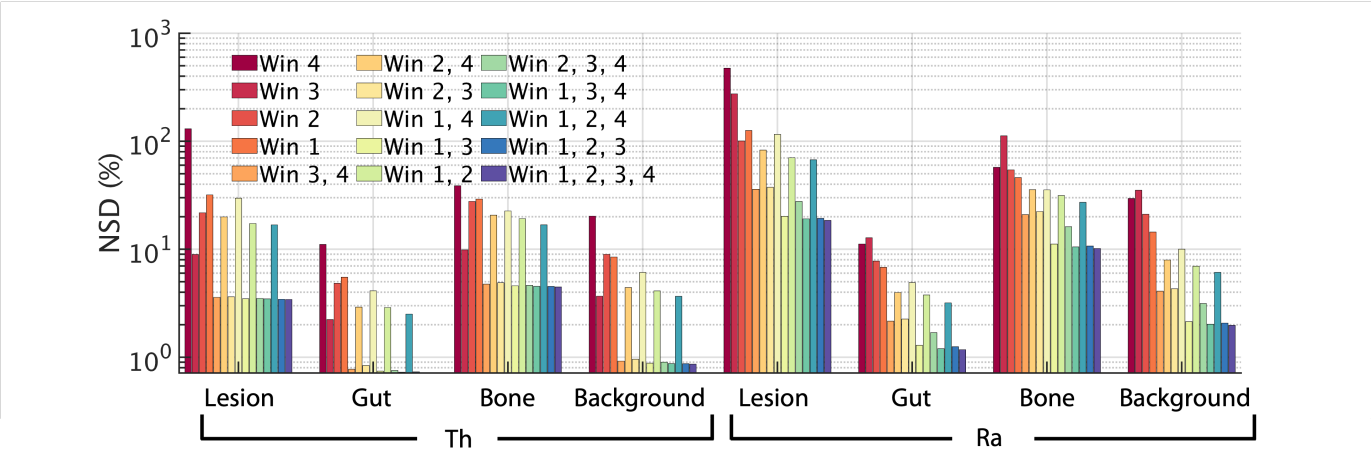


Fig. 3: CRLB-derived NSD values for estimating regional uptake of $^{227}\mathrm{Th}$ and $^{223}\mathrm{Ra}$ using different combinations of energy windows.

### B. Results

Table II presents the NB and NRMSE values for the estimated regional uptake of $^{227}\mathrm{Th}$ and $^{223}\mathrm{Ra}$ obtained in this experiment. It was observed that the LC-QSPECT method yielded NB and NRMSE values exceeding 100% in the estimation of $^{223}\mathrm{Ra}$ uptake across all regions. Additionally, the proposed MEW-PDQ method significantly outperformed the LC-QSPECT method.

## V. CRLB WITH DIFFERENT ENERGY WINDOW COMBINATIONS

### A. Experiments

To supplement the evaluations in Sec. III C 1) d) of the main manuscript, we conducted an additional analysis to assess the impact of using more energy window combinations on the theoretical lower bound of estimated regional uptake variance. For this purpose, we calculated the CRLB for all possible combinations of the four energy windows depicted in Fig. 1 of the main manuscript. The same typical patient phantom was considered in this experiment and the CRLB-derived NSD values were calculated as described in Section III C 1) d) of the main manuscript.

### B. Results

Fig. 3 shows the CRLB-derived NSD values for estimating regional uptake of $^{227}\mathrm{Th}$ and $^{223}\mathrm{Ra}$ using different combinations of energy windows. We observe that using all four energy windows resulted in the lowest CRLB-derived NSD value, consistent with the data processing inequality principle [10].

## REFERENCES


[1] M. Ljungberg and S.-E. Strand, "A Monte Carlo program for the simulation of scintillation camera characteristics," *Comput Methods Programs Biomed*, vol. 29, no. 4, pp. 257–272, 1989.

[2] M. B. Toossi, J. P. Islamian, M. Momennezhad, M. Ljungberg, and S. Naseri, "SIMIND Monte Carlo simulation of a single photon emission CT," *J Med Phys*, vol. 35, no. 1, p. 42, 2010.

[3] M. Morphis, J. A. van Staden, H. du Raan, and M. Ljungberg, "Validation of a SIMIND Monte Carlo modelled gamma camera for Iodine-123 and Iodine-131 imaging," *Heliyon*, vol. 7, no. 6, p. e07196, 2021.

[4] Z. Li *et al.*, "A Projection-Domain Low-Count Quantitative SPECT Method for $\alpha$-Particle-Emitting Radiopharmaceutical Therapy," *IEEE Transactions on Radiation and Plasma Medical Sciences*, vol. 7, no. 1, pp. 62–74, 2023.

[5] T. Merlin *et al.*, "CASToR: a generic data organization and processing code framework for multi-modal and multi-dimensional tomographic reconstruction," *Phys Med Biol*, vol. 63, no. 18, p. 185005, 2018.

[6] E. C. Frey and B. Tsui, "A new method for modeling the spatially-variant, object-dependent scatter response function in SPECT," in *1996 IEEE Nucl Sci Symp Conf Rec*, vol. 2. IEEE, 1996, pp. 1082–1086.

[7] M. Soret, S. L. Bacharach, and I. Buvat, "Partial-volume effect in PET tumor imaging," *J Nucl Med*, vol. 48, no. 6, pp. 932–945, 2007.

[8] O. G. Rousset, Y. Ma, and A. C. Evans, "Correction for partial volume effects in PET: principle and validation," *J Nucl Med*, vol. 39, no. 5, pp. 904–911, 1998.

[9] H. H. Barrett and K. J. Myers, *Foundations of image science*. John Wiley & Sons, 2013.

[10] N. J. Beaudry and R. Renner, "An intuitive proof of the data processing inequality," *arXiv preprint arXiv:1107.0740*, 2011.